Solidification behavior and texture of 316L austenitic stainless steel by laser wire directed energy deposition

Olivia DeNonno[a], Alec Saville[a,b], Jake Benzing[b], Jonah Klemm-Toole[a], Zhenzhen Yu[a],
[a] Colorado School of Mines, Golden, CO, USA
[b] National Institute of Standards and Technology, Boulder, CO, USA

Corresponding author.
E-mail address: zyu@mines.edu (Z. Yu)

Abstract

The solidification behavior and crystallographic texture of 316L austenitic stainless steel builds fabricated via laser-wire directed energy deposition additive manufacturing (AM) were investigated. Shielding gas set-up and build type (single-track vs. multi-track) were varied, which led to changes in the solidification conditions and the final build compositions. Primary δ-ferrite solidification is predicted based on equilibrium thermodynamic predictions of the bulk feedstock composition. However, the increased solidification velocity of the AM process promotes a solidification mode transition from primary δ-ferrite to primary austenite. Skeletal δ-ferrite and lathy δ-ferrite associated with primary δ-ferrite solidification and interdendritic δ-ferrite associated with primary austenite solidification were observed among the laser-wire directed energy deposition walls. Skeletal and interdendritic δ-ferrite exhibited a (001)δ // (001)γ parallel relationship with austenite and a {001} solidification texture aligned with the build direction for both austenite and δ-ferrite. Lathy δ-ferrite exhibited a Kurdjumov-Sachs orientation relationship, $(101)\delta//(1\bar{1}1)\gamma$ with austenite due to austenite nucleation in the solid-state. It is shown that the solidification behavior of AM 316L is accurately represented by as-built composition data and a dendrite growth model, which combined, encompasses the compositional and solidification condition impacts on the solidification pathway.

Keywords:
Directed energy deposition
Solidification
Crystallographic texture
Stainless steel
Dendrite tip undercooling

1. Introduction

Additive manufacturing (AM) is a layer-by-layer deposition process characterized by steep thermal gradients, and large cooling rates and solidification velocities resulting in unique final microstructures. Metal AM processes are typically defined by the primary heat source, *i.e.,* arc, laser, electron beam, as well as the feedstock delivery method and material type giving rise to processes like laser powder bed fusion (PBF-LB) [1], laser wire directed energy deposition (DED-LB) [2] and wire arc directed energy deposition (DED-Arc) [3]. Powder bed processes typically produce complex and intricate parts, while DED processes produce large-scale parts that require post build machining to a final tolerance [4,5]. Wire based processes utilize commercial welding wires that can be procured at substantially lower costs than powders and employ high deposition rate process parameters, resulting in both cost and time savings [4,6].

The layer-by-layer deposition in a wire-based AM process can be equated to a multi-pass welding process, in which similar thermal conditions exist between the two processes. As a result, alloys that are traditionally considered weldable, *i.e*., easily welded without cracking, are considered suitable for AM. Austenitic stainless steels represent a large class of weldable alloys known for good corrosion resistance, high toughness over a range of temperatures, and moderate elevated temperature strength, making them widely used throughout the energy, chemical, and nuclear industries [7,8]. 300 series austenitic stainless steel such as Types 316L and 304 have been widely studied across AM processes with research related to process parameter optimization and its impact on microstructure [5,9–11], mechanical property evaluation [12–15] and corrosion behavior [16–18].

The microstructure evolution of AM stainless steel is impacted by initial feedstock composition as well as AM process parameters which can have a great impact on elemental loss or gas element absorption in the as-built components. For instance, Table 1 compares the 316L filler wire composition to the ASTM A240 standard, and also summarizes the as-built compositions as a function of building methods in this work. Variations in alloy compositions, such as nickel, manganese, carbon, and nitrogen which stabilize austenite, can lead to considerable variations in the primary solidification mode (i.e., the phase that solidifies first from the liquid) and the subsequent microstructure evolution [19]. During the welding of stainless steel, iron, chromium, nickel, and manganese are the main elements found in the vapor plume

[20–22]. Hawk calculated the partial pressure of gaseous elements in vapor plumb for 304L stainless steel and found that iron, nickel, and chromium have the largest partial pressure as those are the most abundant elements in stainless steel [23]. Collur *et al*. observed iron, manganese, and chromium as the dominant species in plasma during laser welding of AISI 201 stainless steel, matching Hawk's calculations [20].

The solidification pathway encompasses the primary solidification mode and any subsequent solid-state phase transformations and dictates the final microstructure of an AM part. There are four primary solidification modes for austenitic stainless steels which consist of A – primary austenite, AF – primary austenite with secondary δ-ferrite, FA – primary δ-ferrite with secondary austenite, and F –primary δ-ferrite [24–26]. The morphology of δ-ferrite is often used to characterize the solidification pathway of stainless steels. Constitution diagrams such as the Schaeffler and DeLong diagrams have been often used as a convenient tool to predict the final microstructure of welds based on filler or alloy composition in the welding society [19]. Within the 316L composition range, both primary δ-ferrite and primary austenite solidification are possible, as illustrated by a calculated Fe-Cr-Ni isopleth (70 wt% Fe) shown in Fig. 1a, where the composition range of 316L spans into the two-phase γ + L region and across to the δ + L region. The isopleths in Fig. 1 were generated using Thermo-Calc© software version 2022b (TCFE12 database) where phases besides face-centered cubic (FCC), body-centered cubic (BCC), and liquid were suppressed. Therefore, rigid microstructure control for AM 316L can be challenging considering the variation in the solidification pathway, which is greatly impacted by alloy composition.

Table 1 - Elemental composition (% mass fraction) of 316L wire feedstock, deposited DED material, and UNS 316L standard and as-built hardness.

	C	N	Si	Cr	Ni	Mn	Mo	Fe[c]	Cr_{eq}/Ni_{eq}[19]	Hardness (HV)
316L Standard[d]	0.03	0.10	0.75	16.0— 18.0	10.0 – 14.0	2.00	2.0 – 3.0	Bal	-	-
316L Wire Feedstock	0.01	0.064[b]	0.53	18.35	11.22	1.48	2.30	66.1	1.51	-
Single-Track - Torch	0.01	0.0732[a]	0.43	18.04	11.46	1.23	2.56	66.2	1.46	183 □ 5
Multi-Track - Torch	0.01	0.0815[a]	0.20	17.60	14.72	0.60	2.60	64.2	1.15	187 □ 7
Single-Track - Updated	0.01	0.0677[a]	0.74	19.01	14.45	1.19	2.53	62.0	1.30	185 □ 4
Multi-Track - Updated	0.01	0.0691[a]	0.51	18.43	11.56	1.41	2.62	65.4	1.49	190 □ 5

[a] From separate nitrogen combustion testing per ASTM E1019-18
[b] From Harris Product Group Material Test Report
[c] Calculated from summed composition of other elements
[d] 316L Standard – Per ASTM A240, maximum, unless range or minimum specified

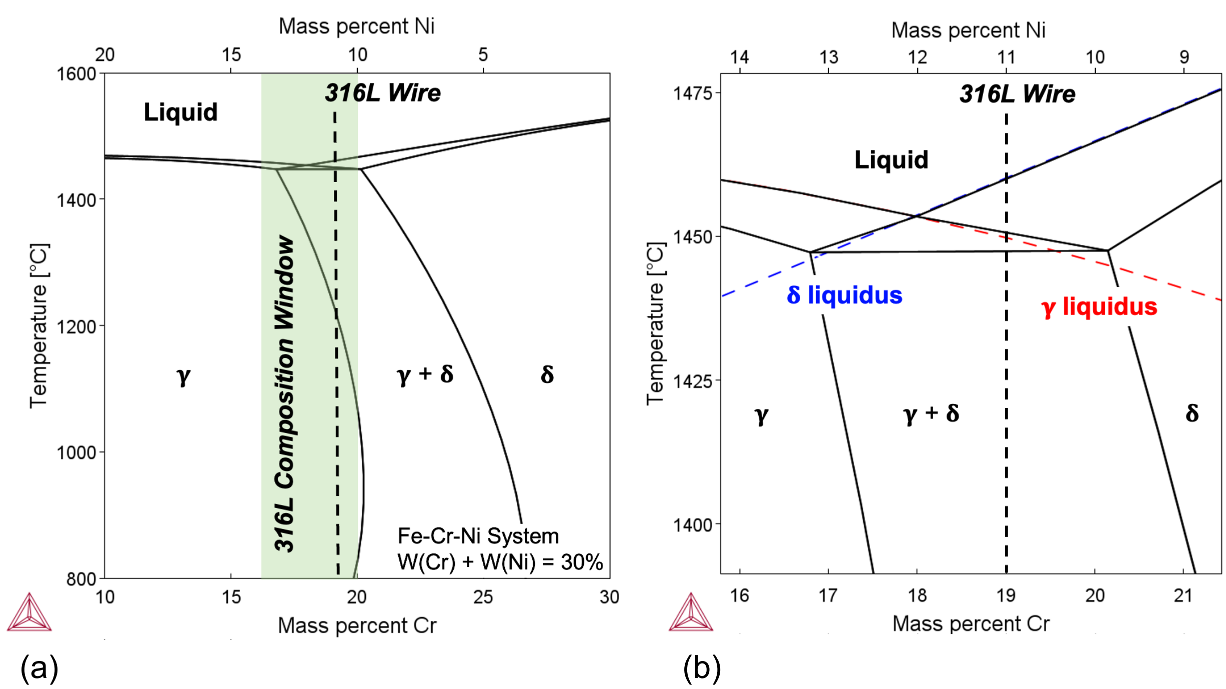

Fig. 1. (a) Fe-Cr-Ni isopleth fixed at 70 wt% Fe with (b) enlarged section showing metastable liquidus lines for austenite and δ-ferrite.

AM process parameters are considered another important factor in microstructure evolution. A completely austenitic microstructure is typically reported for most PBF-LB builds of 316L with cooling rates on the order of 10^5 K/s [27,28], while for slower solidification velocity processes like DED-LB or DED-Arc where cooling rates are on the order of $10^2 – 10^3$

K/s, a two-phase microstructure of austenite and δ-ferrite is observed [4,14,16]. As solidification velocity increases, as observed for faster solidification processes like PBF-LB compared to DED-LB and DED-ARC processes, dendrite tip undercooling is impacted in a manner that can lead to the formation of non-equilibrium microstructures [19,29]. Specifically, fully austenitic microstructures can form under high solidification velocities in alloy compositions expected to form a two-phase (δ and γ) microstructure under equilibrium conditions. This was first detected with the introduction of high energy density beam welding processes such as laser and electron beam, where a shift in solidification mode from primary δ-ferrite to primary austenite was observed as solidification velocity increased [24–26,29]. Schaeffler and DeLong diagrams were originally developed for fusion welding solidification conditions in steels, and therefore composition was the only variable used to determine the final microstructure. More recently, microstructure maps considering both composition and solidification velocity were developed to account for solidification mode shifts as a result of increased solidification velocities [24,29]. Note that these microstructure maps were generated using experimental data before CALPHAD methods were available to calculate and predict thermodynamic and kinetic properties for multicomponent material systems. As such, there are opportunities to utilize thermodynamic data from CALPHAD to aid in a more efficient prediction of the solidification behavior of AM builds.

Although two-phase δ-ferrite and austenite microstructures are observed in DED-LB and DED-Arc AM 316L, typically only the crystallographic texture of the austenite has been discussed with no comment regarding the texture of the primary solidifying δ-ferrite phase [14,30]. A strong {001} texture of the austenite aligned with the build direction is generally reported, which is attributed to the fast growth direction of dendrites in cubic systems during solidification [11,28,31]. However, austenite is not necessarily the primary solidifying phase, thus orientation relationships between austenite and the primary solidifying δ-ferrite phase are needed to interpret the observed texture. For example, within austenitic stainless steel welds, a (001)δ // (001)γ orientation relationship (OR) is reported between skeletal δ-ferrite and austenite, while for lathy δ-ferrite, the Kurdjumov-Sachs (K-S) OR is reported between δ-ferrite and austenite [26,32,33]. The K-S OR describes a pair of close-packed planes that are parallel and the corresponding parallel directions typically for an FCC to BCC transformation. The K-S OR between lathy δ-ferrite and austenite can result in higher coherency boundaries, which are less potent nucleation sites for sigma phase to form compared to the incoherent boundaries between skeletal δ-ferrite and austenite [33]. Controlling the solidification microstructure and subsequent solid-state transformations is key to preventing the formation of deleterious secondary intermetallic phases like sigma phase. However, very limited in-depth studies have been conducted on texture evolution as a function of the solidification pathway in AM austenitic stainless steels, where δ-ferrite of various morphologies is observed.

In this work, the solidification behavior and crystallographic texture of 316L austenitic stainless steel builds produced via the DED-LB AM process with various shielding gas arrangements and build types will be thoroughly investigated through metallurgical characterizations and dendrite growth modeling. This work aims to reveal the impact of solidification conditions and compositional variation on solidification behavior and crystallographic texture that result in a variety of as-built microstructures of AM 316L stainless steel.

2. *Experimental Methodology*

2.1 Material Production

DED-LB equipment was used to fabricate single and multi-track walls using 0.89 mm (0.035 in) diameter 316L gas metal arc welding wire. The experimental DED-LB equipment, shown in Fig. 2a, is comprised of a three-axis machining center outfitted with a 4 kW IPG[1] ytterbium fiber laser (YLS-4000), an IPG Weld D30 series welding head, and a Miller 70 Series wire feeder. The fiber laser was operated in continuous wave mode with a wavelength of 1070 nm. An optris PI 08M thermal camera, which traveled in line with the laser head, was added to the set-up to monitor the builds during the fabrication process.

Footnote:

[1] Commercial equipment, instruments, or materials are identified only in order to adequately specify certain procedures. In no case does such identification imply recommendation or endorsement by the National Institute of Standards and technology, no does it imply that the products identified are necessarily the best available for the purpose.

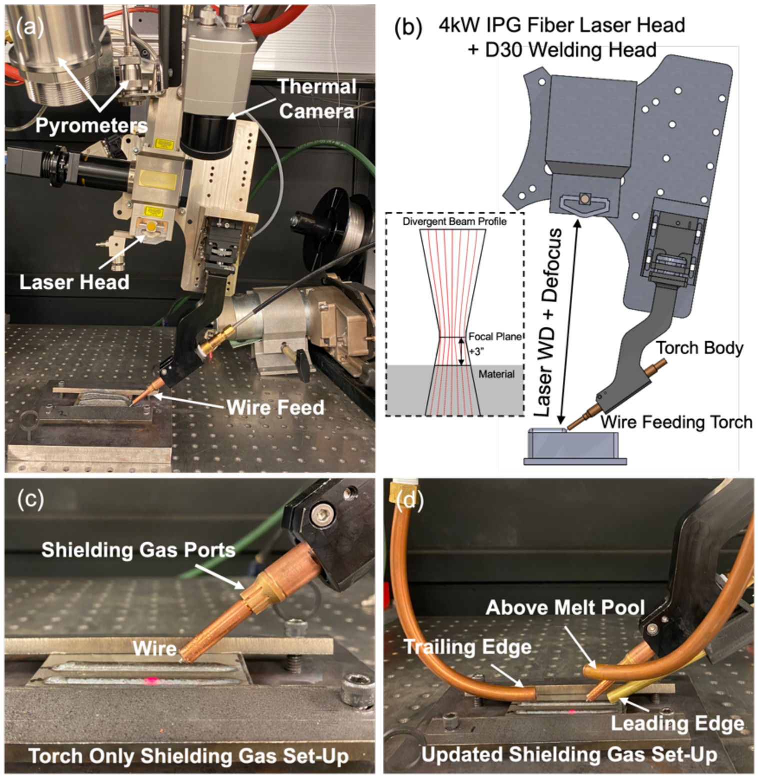

Fig. 2. DED-LB experimental equipment used to build AM 316L single and multi-track walls. (a) overview of DED-LB equipment, (b) schematic highlighting laser defocus necessary for conduction mode melting, (c) torch only shielding gas set-up, and (d) updated shielding gas set-up.

Single beads were deposited initially on 316L baseplates to determine process parameters such as laser power, scan speed, wire feed speed, and laser defocus distance for the fabrication of larger scale DED-LB builds. The initial deposition of single beads at the manufacturer's specified welding head optic working distance of 159 mm resulted in deep and narrow melt pools associated with keyhole formation. The beam profile at the manufacturer's specified working distance of 159 mm is fully in focus and results in the smallest laser spot size. Attempts to address the keyholing issue by varying process parameters such as decreasing laser power or increasing laser scan speed resulted in insufficient heat input to melt the wire, indicating the laser beam spot size at the manufacturer's specified working distance of 159 mm was too small to create a melt pool of proper size and shape for a DED-LB AM process.

Changing the working distance*, i.e.,* moving the focal plane of the laser, is found to be the easiest method to vary laser beam spot size. By moving the focal plane above the substrate material, the laser beam profile becomes divergent, which effectively produces shallow and wide melt pools associated with conduction mode melting [34]. The defocusing methodology was evaluated, and it was found that a 76.2 mm (3 in) positive defocus above the specified focal plane resulted in a desired shallow, 1.2 mm deep and 4.5 mm wide, melt pool shape, where the wire feedstock could easily be deposited. Process parameters used to fabricate single-track (single bead wide) and multi-track (three bead wide) DED-LB walls are given in Table 2. A schematic of the DED-LB set-up with the divergent laser beam profile is illustrated in Fig. 2b.

Table 2 - Process parameters for DED-LB builds.

Processing Parameter	Value
Nominal Laser Power (W)	4000
Travel Speed (mm/s)	10
Wire Feed Speed (mm/s)	90
Wire Diameter (mm)	0.89 (0.035in)
Deposition Rate (kg/h)	1.45
Laser Defocus (mm)	76.2 (3in)
Shielding Gas Flow Rate (cubic feet per hour)	15
Hatch Spacing* (mm)	2.5

*only applicable for multi-track walls

The DED-LB builds were fabricated using two different shielding gas configurations shown in Fig. 2c and Fig. 2d, in which ultra high purity (99.999%) argon was used as the shielding gas for both set-ups. The torch only shielding gas set-up utilizes only a Binzel torch body with a custom machined copper contact tip to feed 0.89 mm (0.035 in) wire. The shielding gas flows through the shielding gas ports indicated in Fig. 2c. Initial DED-LB builds were fabricated using the torch only shielding gas set-up, and large gas porosity predominantly located near the top layer of the builds was observed indicating the torch only set-up provided insufficient protection of the melt pool during the build process. Improvements were made to the shielding gas set-up, as shown in Fig. 2d, to reduce the amount of porosity and oxidation. The updated shielding gas set-up consists of the same torch as shown in Fig. 2c, but with the addition of leading edge, trailing edge, and above melt pool shielding to create a shielding gas envelope around the melt pool. Reductions in size and amount of porosity were observed for DED-LB builds fabricated with the updated shielding gas set-up.

2.2 Microstructure Characterization

Sections from the approximate middle of the DED-LB builds comprising bulk layers and the top layer of the build were mounted in copper containing conductive mounting compound for scanning electron microscope (SEM) characterization. Samples were metallographically prepared using 800 and 1200 grit grinding paper, 9 μm, 6 μm, 3 μm, and 1 μm diamond suspension, and swab etched using glyceregia (3:2:1 glycerine:HCl:HNO_3) for 2 minutes – 3 minutes. Characterization of microstructure morphology and phases was performed on a Tescan S8000 SEM equipped with an EDAX Octane Elect Plus energy dispersive spectrometer (EDS). The bulk chemical composition of each of the DED-LB builds as well as 316L wire feedstock was characterized with spark atomic emission spectrometry according to ASTM E1086-14 [35] and the nitrogen content was characterized with inert gas fusion and thermal conductivity detection method according to ASTM E1019-18 [36]. The results of the chemical composition analysis for representative DED-LB builds and feedstock wire are presented in Table 1 [37]. Also reported in Table 1 is the as-built microhardness for representative walls of each condition. Vickers microhardness measurements were collected using a LECO automated hardness testing system (AMH55) under 500 gf with 10 second dwell and 500 μm spacing between indents.

Analysis of crystallographic texture was performed using electron backscatter diffraction (EBSD) on a JEOL 7000F field-emission SEM (FE-SEM) equipped with an EDAX Hikari Pro EBSD detector. Samples were prepared in the same manner as stated above with the addition of a final 0.06 μm colloidal silica polishing step on a Buehler 2 vibroMet for 18 – 24 hours. No chemical etching was performed on the EBSD samples. Large-scale EBSD scans were performed as well and each EBSD tile was generated with a 5% overlap and tiles were stitched together using commercially available software. All EBSD scan data was input into MATLAB plugin MTEX version 5.6.1 where pole figures and inverse pole figure maps were generated to analyze the impact of solidification morphology on build texture.

3. Results

3.1 Microstructure Characterization and Solidification Sequence

Three microstructure morphologies, skeletal δ-ferrite, lathy δ-ferrite, and interdendritic δ-ferrite that have been defined throughout weld metallurgy literature [19,24–26] were identified within the single-track and multi-track DED-LB builds fabricated with the torch only and updated shielding gas set-up. δ-ferrite is present in the microstructure of all the DED-LB builds indicating either FA or AF-type solidification occurred. Skeletal and lathy δ-ferrite form as a result of FA-type solidification while interdendritic δ-ferrite forms as a result of AF-type solidification.

For single-track walls fabricated with the torch only shielding gas set-up, skeletal δ-ferrite morphology was observed throughout the bulk of the wall, as shown in Fig. 3a and Fig. 3b. At the last deposition layer, the very top of the wall, interdendritic δ-ferrite was observed as shown in Fig. 3d and Fig. 3e. Every layer of the DED-LB builds except the last layer deposited, considered here the top layer, experiences repeated remelting and resolidification as subsequent build layers are deposited. This remelting results in the destruction of the as-deposited microstructure on top of the melt pool. The top of the melt pool is only preserved in the top layer of the build, where a shift in δ-ferrite morphology was observed for single-track walls fabricated with the torch only shielding gas set-up.

In the bulk of the single-track wall (Fig. 3c), EDS analysis demonstrated that δ-ferrite is rich in ferrite stabilizing elements like chromium and molybdenum and depleted in nickel, an austenite stabilizer [19]. An increase in nickel content is observed in between the retained skeletal δ-ferrite, signified by yellow dashed line in Fig. 3b and labeled as nickel arch in Fig. 3c. The increase in nickel content in the interdendritic region indicates the microstructure evolved via FA-type solidification with the primary skeletal δ-ferrite only remaining at the original dendrite core location after the δ-ferrite to austenitic transformation. During solidification, δ-ferrite dendrites grow into the liquid, and nickel and other austenite stabilizing elements are rejected by the moving δ-ferrite/liquid boundary to the liquid interdendritic region. Secondary austenite forms in the chemically segregated nickel-rich interdendritic liquid between the δ-ferrite dendrite once the temperature drop below the metastable austenite liquidus, the red dashed line in Fig. 1b. [26]. As the temperature continues to decrease, the stability of austenite increases at the expense of δ-ferrite, and austenite consumes δ-ferrite via a solid-state phase transformation until it reaches the chromium and molybdenum enriched dendrite cores. Because the cooling rate is high, DED-LB processes report a cooling rate around $10^2 – 10^3$ K/s [4], the diffusion controlled solid-state phase transformation is limited, and the δ-ferrite dendrite cores enriched in ferrite stabilizing elements are chemically stabilized, resulting in skeletal δ-ferrite retained at the original dendrite cores to room temperature.

At the top layer of the single-track wall (Fig. 3f), EDS analysis revealed an absence of a nickel arch between the δ-ferrite. The EDS line scans show local nickel rejection near δ-ferrite formation, as marked out by the black arrows, indicating the formation of interdendritic δ-ferrite via AF-type solidification. During solidification of the microstructure in Fig. 3f, austenite dendrites form first and grow into the liquid, and δ-ferrite stabilizing elements are rejected to the interdendritic region by the moving austenite/liquid boundary. As the austenite dendrites continue to grow into the liquid, continued segregation of ferrite stabilizing elements to the interdendritic region results in sufficient driving force for secondary δ-ferrite to form in the interdendritic region near or at austenite dendrite boundaries. This results in the local rejection of nickel, near the formation of δ-ferrite as indicated by arrows on the EDS line scans (Fig. 3f). Austenite continues to grow into the δ-ferrite as the stable phase, further partitioning ferrite stabilizing elements to the dendrite boundaries, stabilizing the interdendritic secondary δ-ferrite to room temperature [38].

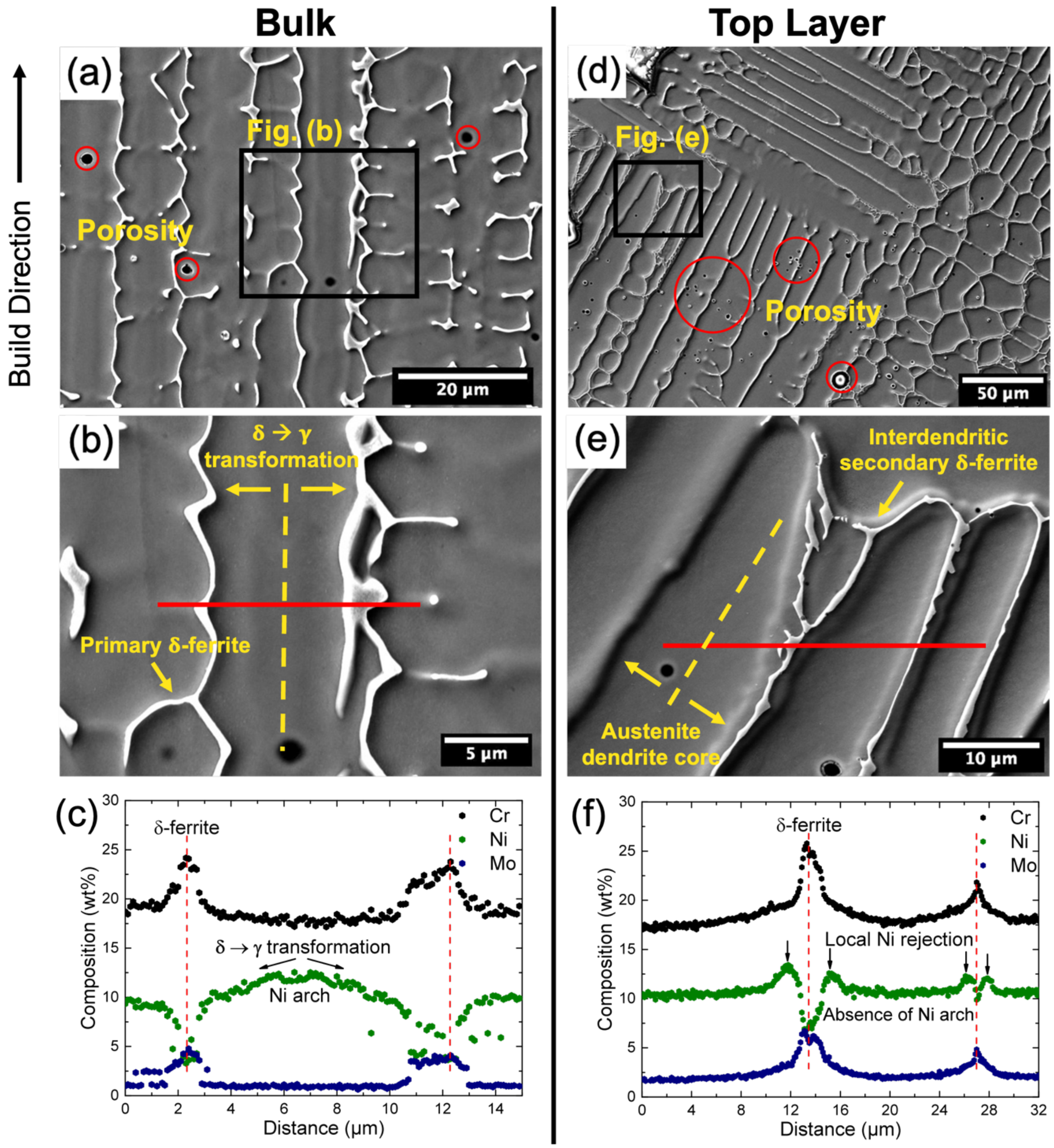

Fig. 3. SEM micrographs and EDS line scans of microstructures morphologies present in single-track walls fabricated with the torch only shielding gas set-up. Microstructure morphologies identified in the wall include (a-b) skeletal δ-ferrite in the bulk, with (c) related EDS lines scan, and (d-e) interdendritic δ-ferrite in the top layer, with (e) related EDS line scan. Gas porosity is circled in (a) and (d).

Multi-track walls fabricated with the torch only shielding gas set-up consist of interdendritic δ-ferrite throughout the bulk (Fig. 4a and 4b) and the top layer (Fig. 4d and 4e) of the walls. EDS analysis of the bulk and top layer microstructure (Fig. 4c and 4f) reveal a similar line scan pattern as the top layer of the single-track wall (Fig. 3f) with local nickel rejection near the formation of interdendritic δ-ferrite. The multi-track walls exhibited consistent AF-type solidification throughout the entirety of the wall, which is a shift in solidification mode from mostly FA-type solidification observed in the single-track wall fabricated with the torch only shielding gas set-up.

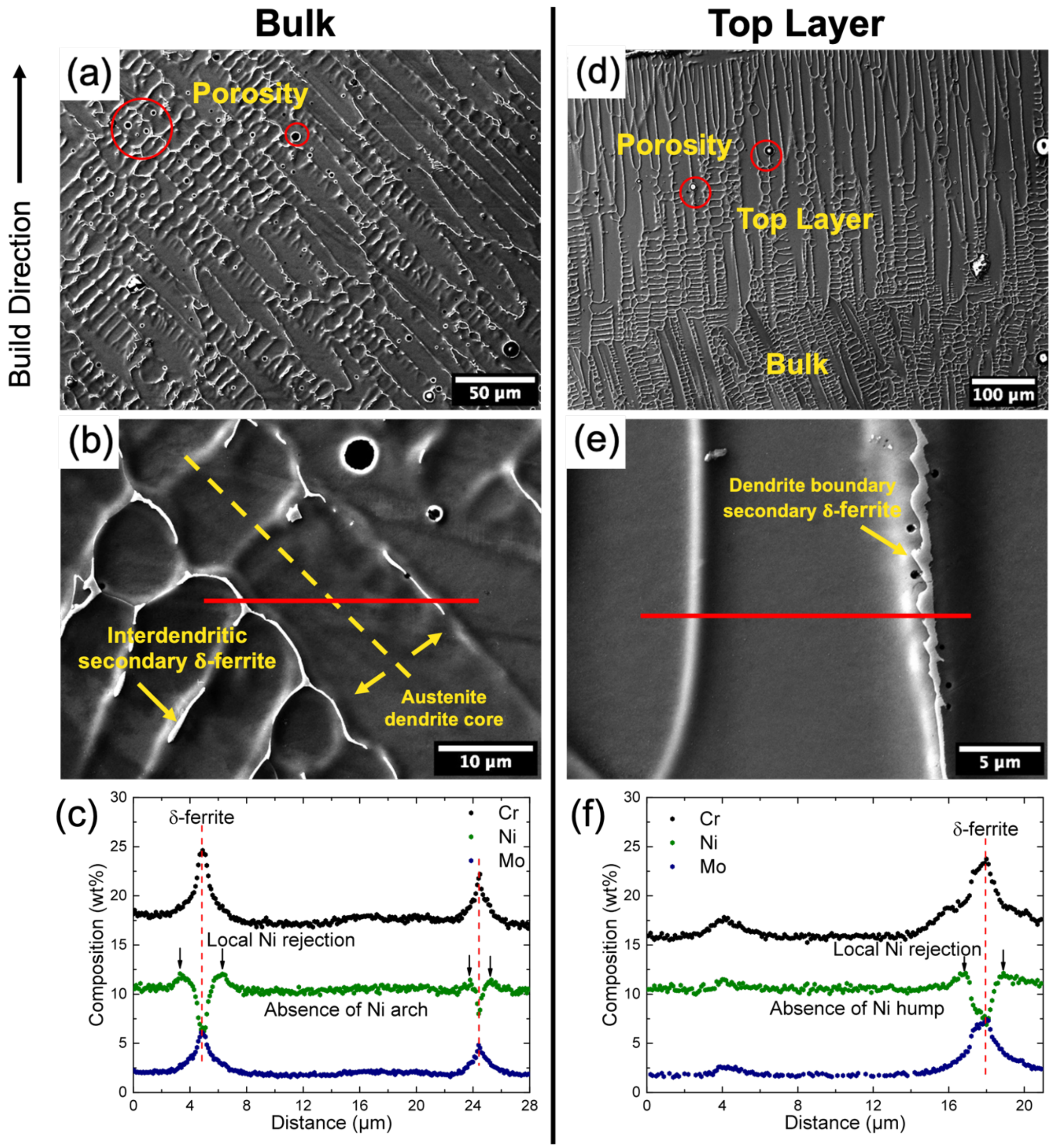

Fig. 4. SEM micrographs and EDS line scans of microstructure morphologies present in the multi-track walls fabricated with the torch only shielding gas set-up. Microstructure morphologies identified in the wall include (a-b) interdendritic δ-ferrite observed in the bulk, with (c) related EDS lines scan, and (d-e) interdendritic δ-ferrite observed in the top layer, with (e) related EDS line scan. Gas porosity is circled in (a) and (d).

Spherical gas entrapment pores are present in the microstructure of the DED-LB builds using the torch only shielding gas set-up, as circled in Fig. 3 and Fig. 4. The pores observed within the DED-LB vary in size from 0.75 μm to as large as 60 μm in diameter, which can impact mechanical performance [39]. As discussed in Section 2.1, the updated shielding gas set-up created a protective gas envelope around the melt pool during fabrication which resulted in single melt tracks with no visible oxidation and greatly reduced pore size. Observed porosity ranging in size from approximately 0.5 μm – 1 μm in diameter, circled in Fig. 5a and Fig. 5d. The change in shielding gas set-up also impacted the microstructure evolution of the walls. The single- and multi-track walls fabricated with the updated shielding gas set-up exhibited the same microstructure morphology where the bulk microstructure of both builds (Fig. 5c and 5f) consists of skeletal δ-ferrite which transitioned to lathy δ-ferrite at the top layer (Fig. 5a, 5b, 5d, 5e), respectively. Both skeletal and lathy δ-ferrite are associated with FA-type solidification indicating the updated shielding gas set-up resulted in a consistent solidification mode regardless of the type of wall.

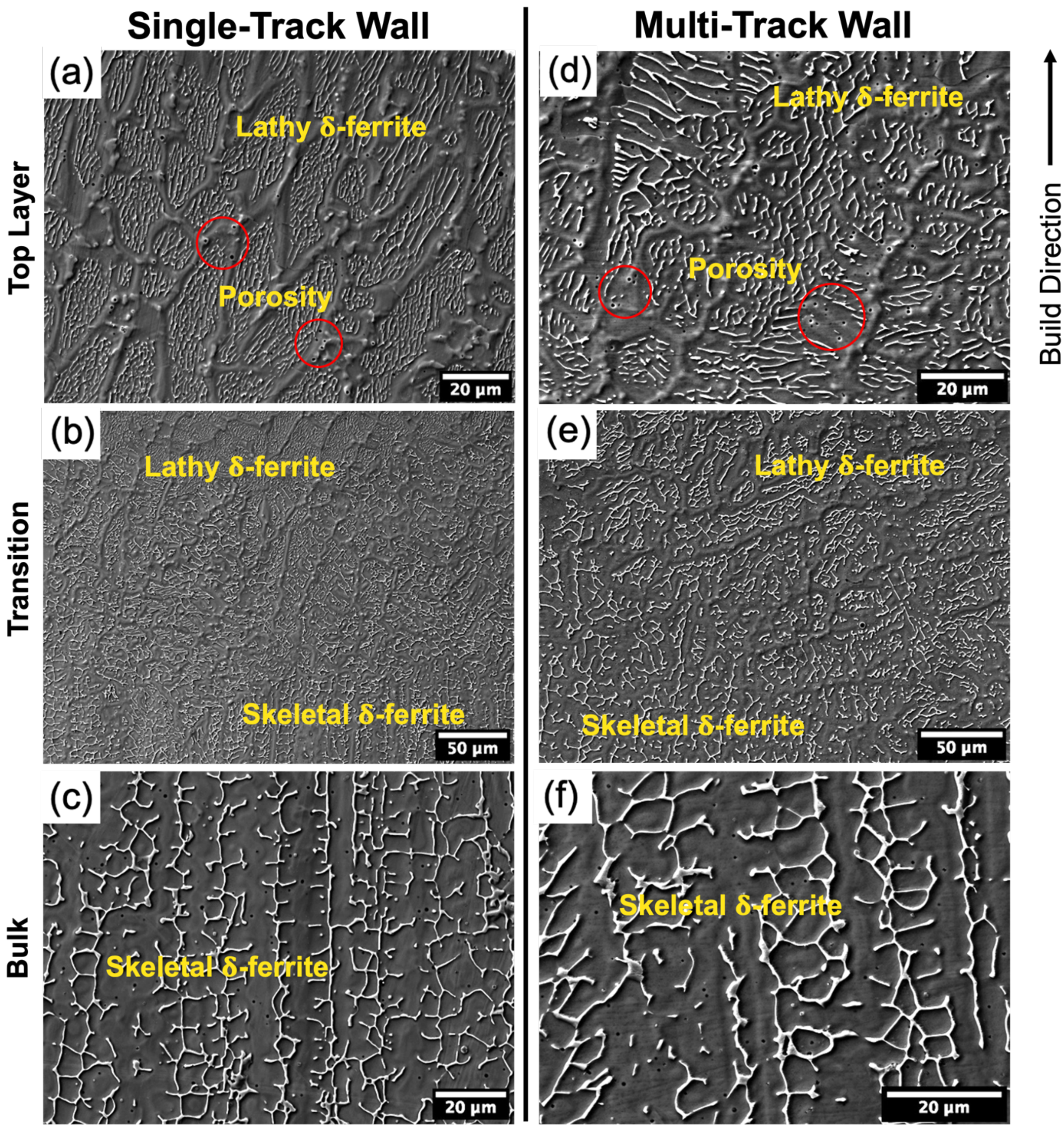

Fig. 5. SEM micrographs of microstructure morphologies present in the single- and multi-track walls fabricated with the updated shielding gas set-up. For both single- and multi-track walls (a, d) lathy δ-ferrite observed at the top layer, with (b, c) transition to skeletal δ-ferrite below the top layer and (c, f) bulk consisting of skeletal δ-ferrite. Gas porosity is circled in (a) and (d).

For skeletal and lathy δ-ferrite, differences in austenite nucleation and growth leads to variations in morphology. For lathy δ-ferrite, austenite nucleation is within the solid δ-ferrite dendrites or at grain boundaries, due to higher cooling rates. The higher cooling rates result in the supersaturation of δ-ferrite dendrites with austenite stabilizing elements leading to plate-like nucleation and growth of austenite in the solid state from δ-ferrite dendrite boundaries resulting in a Widmanstätten morphology of austenite. The lathy morphology is formed from the plate-like austenite that nucleates and grows along a habit plane into the δ-ferrite dendrite cores. It is also likely that some austenite forms in the interdendritic region during cooling from which plate-like austenite can nucleate and grow as well. This mechanism of nucleation and growth has been previously reported within welding literature [33,40,41] and was substantiated by H. Inoue *et al*. with a liquid tin quench of stainless steel welds where Widmanstätten growth of austenite into δ-ferrite resulted in lathy δ-ferrite morphology [32]. The solidification sequence associated with each δ-ferrite morphology discussed above is shown schematically in Fig. 6.

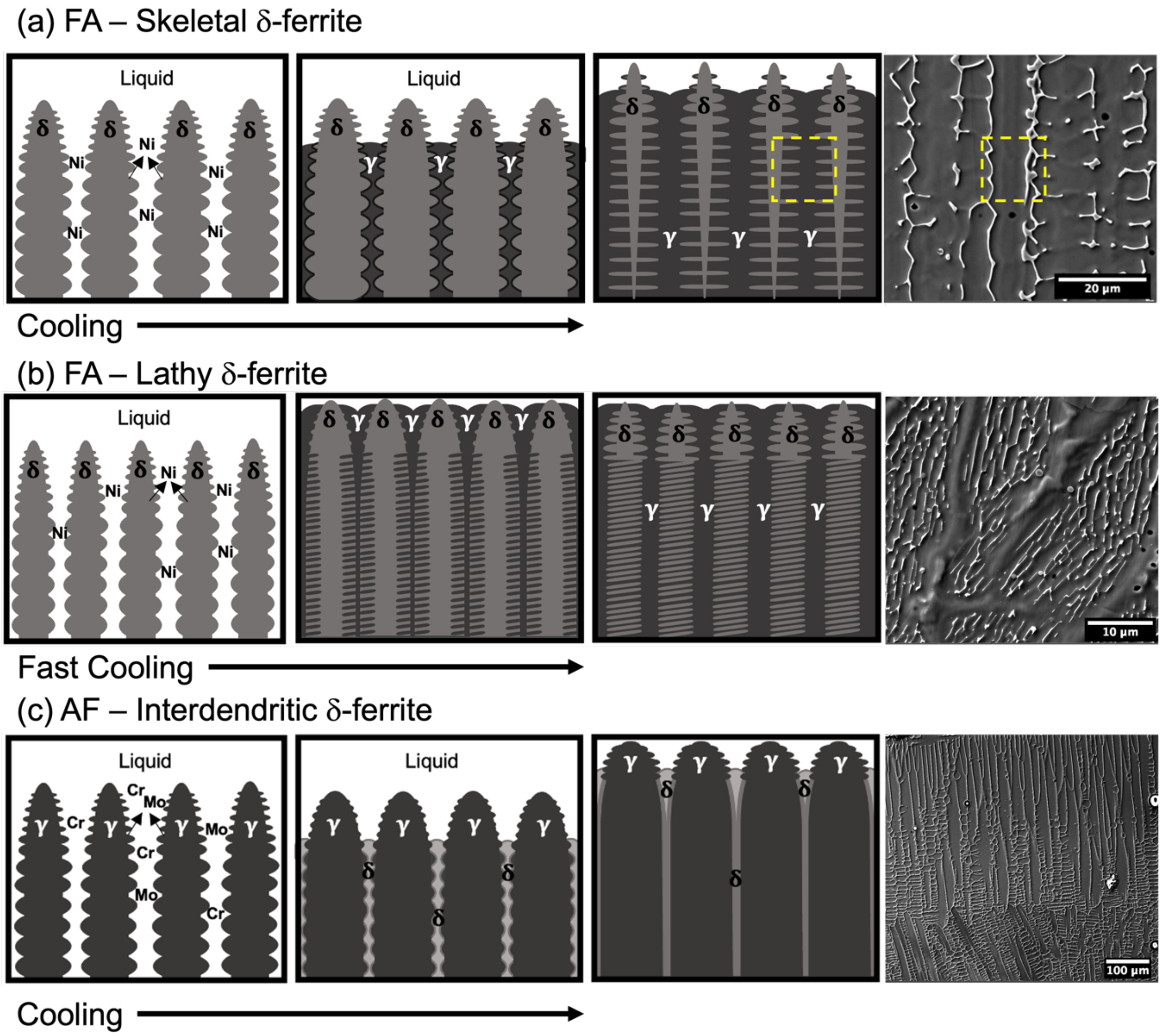

Fig. 6. Schematic diagram of solidification process for (a) skeletal δ-ferrite, (b) lathy δ-ferrite, and (c) interdendritic δ-ferrite [26,42].

3.2 Crystallographic Texture and Orientation Relationships

The epitaxial growth of grains throughout the DED-LB builds resulted in a textured microstructure requiring large-scale EBSD to analyze the bulk texture. Inverse pole figure (IPF) maps of a single-track and multi-track wall fabricated with the torch only shielding gas set-up are shown in Fig. 7. Note that both FCC and BCC were indexed but only the FCC phase is considered in Fig. 7. The z-axis is aligned with the build direction while the x-axis is aligned with DED-LB travel direction. All IPF maps are colorized to the vertical build direction (z-axis). Columnar austenite grains are elongated parallel to the build direction for both walls. A strong {001} texture of the austenite parallel to the build direction, or “solidification” texture, is observed for the single-track wall (Fig. 7a) with 67% of data points within 15° of the (001) pole. A weaker {001} solidification texture is observed for the multi-track wall (Fig. 7b), where only 30% of data points are within 15° of the (001) pole. The addition of laterally deposited beads appears to reduce the texture of the multi-track wall, resulting in a marginally less {001} textured build compared to the single-track wall. For both walls, the {001} solidification texture of austenite is aligned with the build direction and the heat flow direction, shown by the pole figures in Fig. 7c and Fig. 7d. Note the change in reference frame between IPF maps and pole figures where now the build direction (z-axis) is coming out of the page. For both BCC and FCC materials, the preferred growth direction of dendrites is <001> which aligns with the maximum temperature gradient in the build [43].

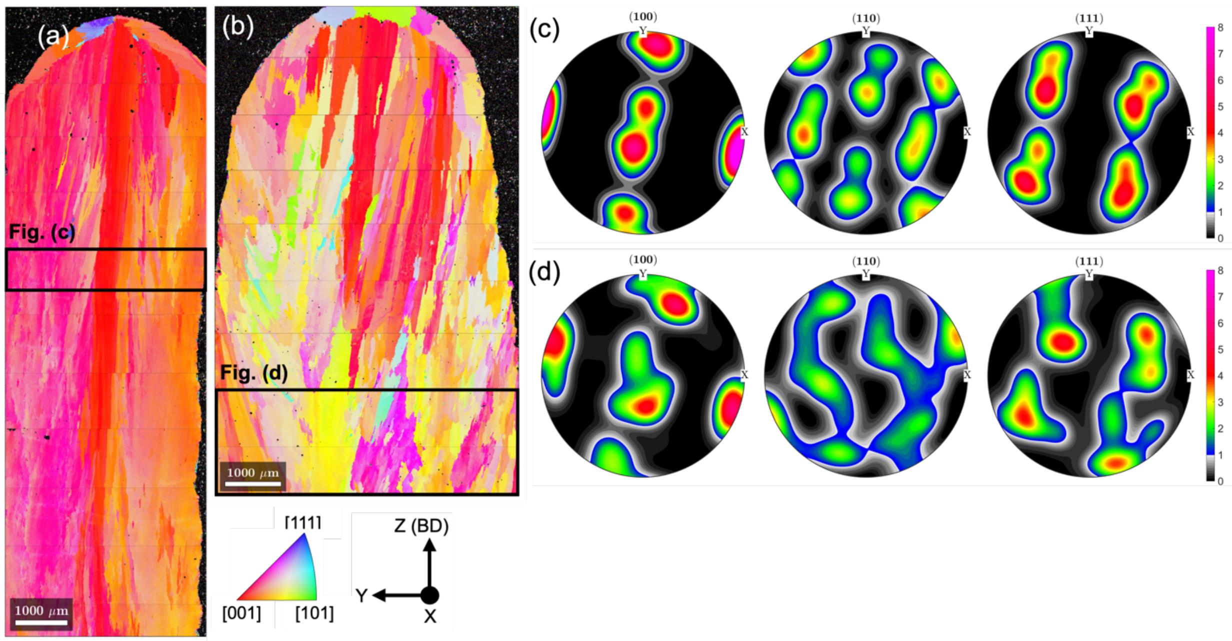

Fig. 7. Large-scale IPF maps (cubic) of (a) single-track and (b) multi-track walls with corresponding austenite pole figures for (c) single-track and (d) multi-track walls. Note the black box on the IPF maps represents the area in which the pole figures were generated from.

IPF maps along with pole figures were generated for each solidification morphology and are presented in Fig. 8 – Fig. 10. The pole figures all have the same reference frame in which the build direction (z-axis) is out of the page, y-axis is vertically up, and x-axis is horizontal from left to right. The pole figure reference frame is different from the IPF map reference frame in which the build direction (z-axis) is always vertically up. Pole figures were generated for both the austenite and δ-ferrite phases and compared in the same plots, Fig. 8d – Fig. 10d, by overlaying the mean δ-ferrite orientations on the top of the austenite pole figures.

A similar orientation between the skeletal δ-ferrite and austenite is indicated by the comparable red coloring of both phases in the IPF map (Fig. 8a). The austenite and δ-ferrite pole figures in Fig. 8b and Fig. 8c demonstrate a strong {001} solidification texture parallel to the build direction, *i.e.*, strong pole intensity in the center of the (100) pole figure aligning with the z-axis. In addition, the (100) pole figure indicates a cube texture, {100}<001> where primary dendrites grow parallel to the heat flow direction, and secondary dendrite growth is fixed to the other <100> directions. This is indicated by the strong pole intensities at the center, X and Y position of the (100) pole figure, corresponding to the [001], [0$\bar{1}$0], and [100] directions. A cube texture is represented by the (100) pole intensities aligning with the faces of a cube, (110) pole intensities aligning with the edges of the cube, and (111) pole intensities aligning with the corners of the cube, thus fixing a cube in space with no rotation possible. Note the cube texture is not perfectly aligned for either austenite or δ-ferrite, *i.e.,* the (100) is not perfectly aligned along the y-axis in Fig. 8b and Fig. 8c, there is a slight rotation about the z-axis, making it a rotated-cube texture. Cube and rotated-cube textures have been reported for FCC AM materials such as IN718, IN625, and 316L [44–46]. Dinda *et al*. showed variations in laser scan pattern can induce specific textures for PBF-LB builds, where a zigzag shaped pattern resulted in a rotated cube texture due to 90° rotation of primary dendrite growth for each subsequent layer [44]. Using neutron diffraction technique on 316L weld material, Blouche *et al*. reported a cube texture for both the austenite and δ-ferrite but noted texture was stronger for austenite comparatively [47].

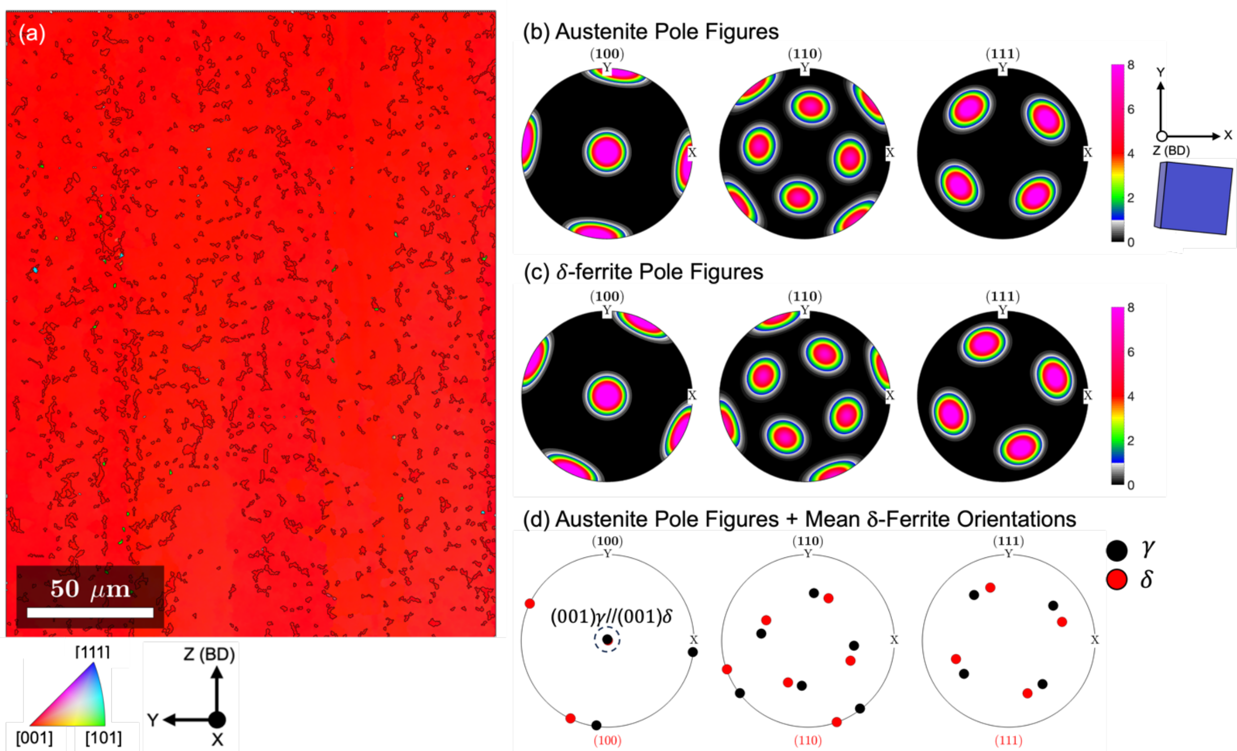

Fig. 8. (a) Skeletal δ-ferrite IPF map and (b) austenite pole figure (c) δ-ferrite pole figure, and (d) austenite pole figure with mean δ-ferrite orientations overlayed showing a parallel relationship between a set of {001} type planes aligned with the build direction.

The overlayed austenite and δ-ferrite pole figure in Fig. 8d shows the [001] direction of δ-ferrite is parallel to the [001] direction of austenite indicating (001)δ // (001)γ. No other additional planes were found to be parallel. During solidification, δ-ferrite and austenite solidify via a parallel growth mechanism in which a set of {001} type planes in both phases are parallel and aligned with the build direction. The other {001} type planes for each phase can rotate freely about the parallel plane resulting in no other matching planes. This parallel growth relationship between δ-ferrite and austenite has been reported in welding literature [32] but is considerably absent from AM literature. Often only the texture of the austenite phase is discussed with no regard to the δ-ferrite phase texture, although δ-ferrite is often the primary solidifying phase.

Interdendritic δ-ferrite has a similar solidification texture to skeletal δ-ferrite (Fig. 9), even though it formed through primary austenite solidification rather than primary δ-ferrite solidification as is the case for skeletal δ-ferrite. The austenite and δ-ferrite pole figures (Fig. 9b and Fig. 9c) indicated a {001} solidification texture relatively aligned with the build direction along with a rotated cube texture about the x-axis compared to the z-axis for the skeletal δ-ferrite case. The $[\bar{1}00]$ direction of δ-ferrite is parallel to the $[\bar{1}00]$ direction of austenite as shown in Fig. 9d indicating a parallel growth mechanism like skeletal δ-ferrite with $(\bar{1}00)\delta$ //$(\bar{1}00)\gamma$. When either δ-ferrite or austenite are solidifying from the interdendritic liquid, a parallel relationship between a set of {001} type planes for δ-ferrite and austenite develops upon solidification and is preserved during cooling.

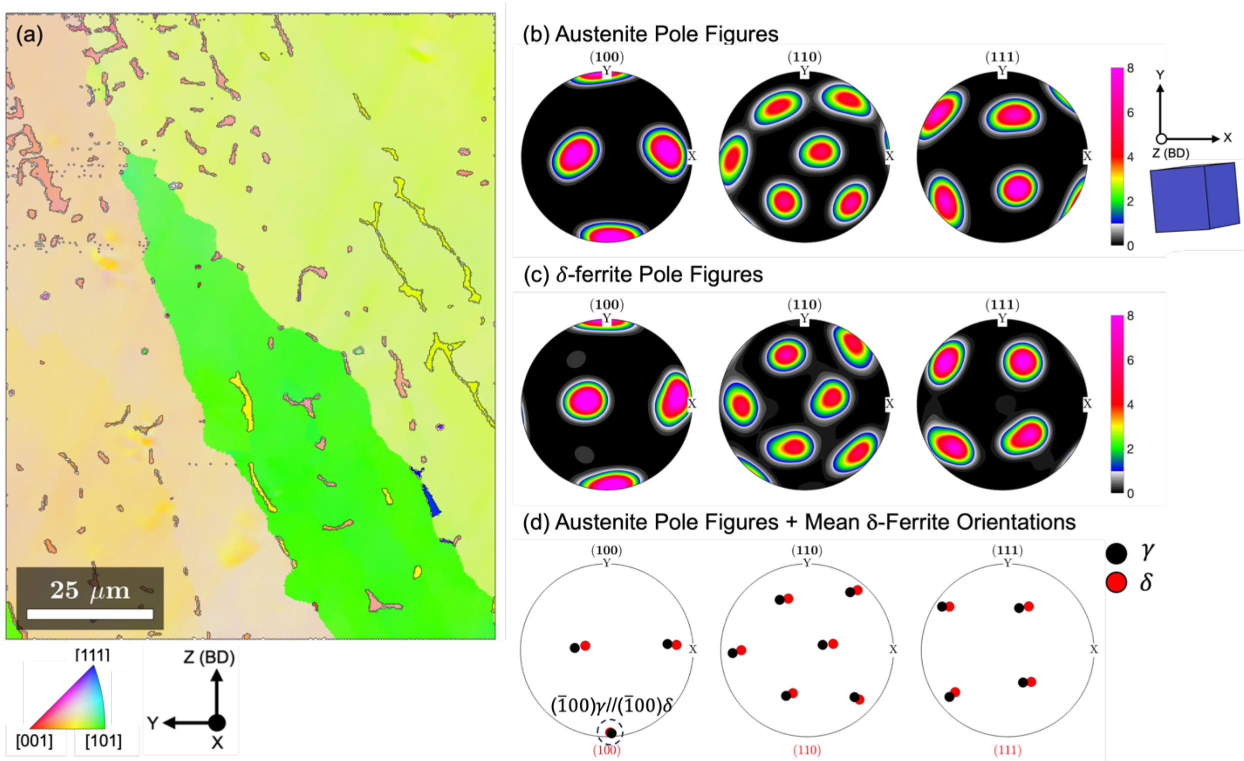

Fig. 9. (a) Interdendritic δ-ferrite IPF map and (b) austenite pole figure (c) δ-ferrite pole figure, and (d) austenite pole figure with mean δ-ferrite orientations overlayed showing a parallel relationship between a set of {001} type planes.

Lathy δ-ferrite is formed in the solid-state via plate-like nucleation and growth of austenite from δ-ferrite dendrite boundaries or the small amount of austenite decorating dendrite boundaries that formed during cooling [40,41]. As a result, the crystallographic OR between δ-ferrite and austenite is no longer a parallel relationship as indicated by the pole figures in Fig. 10b and Fig. 10c. Rather, a Kurdjumov-Sachs (K-S) OR is observed between the δ-ferrite and austenite based on the overlay of the mean (110) δ-ferrite orientations on the (111) austenite pole figure (Fig. 10d). The K-S OR is typically used to describe the crystallographic relationship between austenite transforming to ferrite where a closed-packed FCC plane, {111}, is parallel or near parallel to a closed-packed BCC plane, {110}, with the corresponding closed-packed directions being parallel as well, <110>//<111> [48]. In this case, δ-ferrite is the parent phase while austenite is the product phase. The overlay of pole intensities in Fig. 10d indicates that [101] δ-ferrite direction is parallel to the $[1\bar{1}1]$ austenite direction and the $[\bar{1}\bar{1}1]$ δ-ferrite direction is parallel to the $[0\bar{1}\bar{1}]$ austenite direction, which follows the K-S OR as (101)δ//$(1\bar{1}1)$γ with the $[\bar{1}\bar{1}1]$δ//$[0\bar{1}\bar{1}]$γ. The K-S OR defines a set of parallel planes and directions while the parallel growth relationship for skeletal and interdendritic δ-ferrite only defines a set of parallel planes. A K-S OR between δ-ferrite and austenite for the lathy δ-ferrite morphology has been reported throughout welding literature [26,32,33] but again is missing from AM literature. In addition to a K-S OR, the δ-ferrite and austenite pole figures appear to illustrate a rotated cube texture for both phases with a lack of alignment between a {001} plane and the build direction.

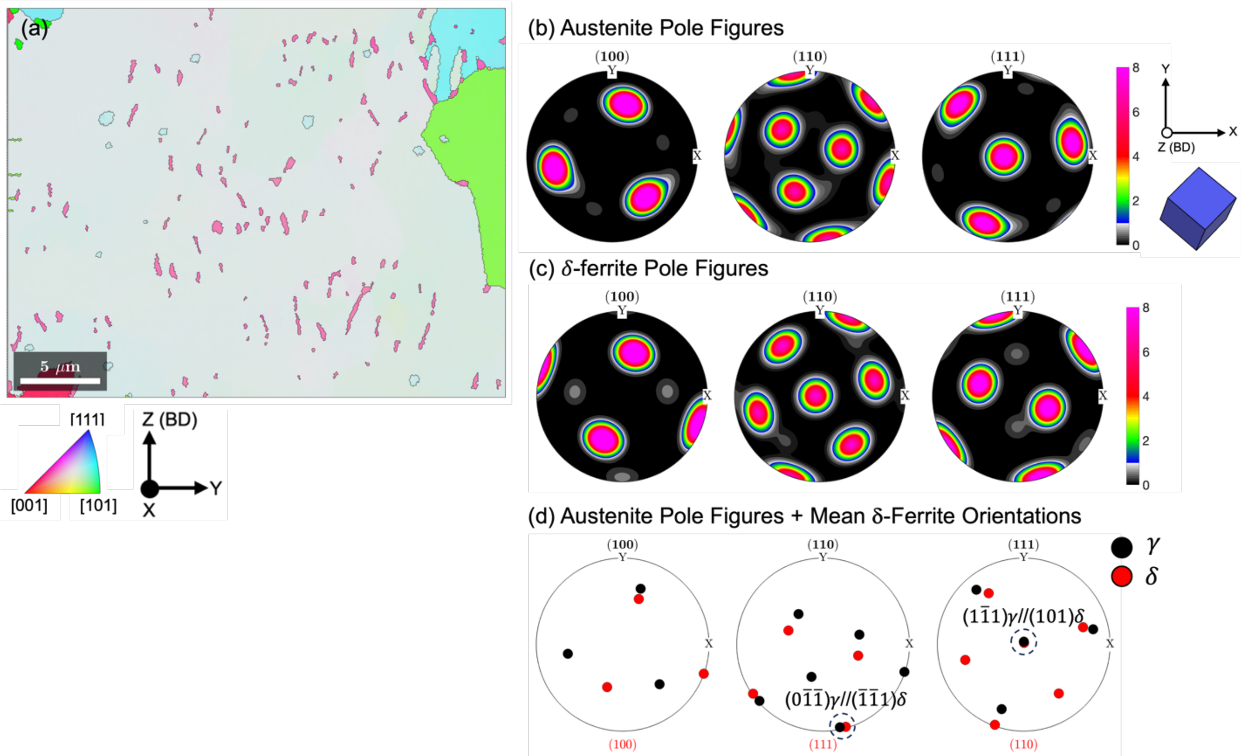

Fig. 10. (a) Lathy δ-ferrite IPF map and (b) austenite pole figure, (c) δ-ferrite pole figure, and (d) austenite pole figure with mean δ-ferrite orientations overlayed showing a K-S OR between δ-ferrite and austenite.

The development of an OR between δ-ferrite and austenite for lathy δ-ferrite morphology leads to a high coherency boundary that minimizes the interfacial energy which is beneficial since the growth of Widmanstätten austenite leads to an increased number of new δ-ferrite/austenite interfaces [32,33]. For the skeletal δ-ferrite case, the OR between δ-ferrite and austenite only specifies one set of parallel planes, resulting in generally incoherent, high-energy boundaries. The planar growth of austenite into δ-ferrite in the skeletal morphology observed by Inoue *et al.* reduces the interfacial energy by minimizing the total interfacial area [32].

4. Discussion

DED-LB builds were fabricated in which the build type, single vs. multi-track, and shielding gas environment, torch only vs. updated, were varied. For the torch only shielding gas set-up, a shift in solidification mode was observed within single-track walls from FA-type solidification in the bulk to AF-type solidification at the top layer. A shift in solidification mode to fully AF-type was observed for the multi-track walls. In comparison, when the shielding gas environment was updated to allow for better shielding of the melt pool, both single-track and multi-track walls exhibited the same solidification mode with fully FA-type solidification, indicating the updated shielding gas set-up resulted in a consistent solidification mode regardless of wall type. Changing the shielding gas set-up impacted both element vaporization loss from the melt pool and cooling rate, leading to differences in solidification mode and microstructural morphology compared to the walls of the same type fabricated with the torch only shielding gas set-up. The microstructure morphology and solidification mode of each of the DED-LB builds described are summarized in Table 3.

Table 3 - Summary of solidification mode and morphology for DED-LB builds.

Shielding Gas Configuration	**Build Type**	**Solidification Mode**		**Solidification Morphology**	
		Bulk	Top Layer	Bulk	Top Layer
Torch only Set-Up	Single-Track	FA	AF	Skeletal δ-ferrite	Interdendritic δ-ferrite
	Multi-Track	AF	AF	Interdendritic δ-ferrite	Interdendritic δ-ferrite
Updated Set-Up	Single-Track	FA	FA	Skeletal δ-ferrite	Lathy δ-ferrite
	Multi-Track	FA	FA	Skeletal δ-ferrite	Lathy δ-ferrite

4.1 Composition Impact on Solidification Mode

Variation in the bulk composition of an alloy or weld is considered to be one of the primary driving forces for shifts in solidification behavior and final microstructure for 300 series austenitic stainless steels. To determine the composition impact on solidification mode, single-axis equilibrium simulations were generated using Thermo-Calc© software version 2022b (TCFE12 database) and the as-built wall compositions (Table 1). The resulting plots are shown in Fig. 11. The primary solidification mode predicted by the single-axis equilibrium simulations matches well with the experimental observations. Primary BCC (δ-ferrite) solidification is predicted for the single-track walls fabricated with the torch only shielding gas set-up (Fig. 11a) as observed throughout the bulk of the wall. The shift in solidification at the top of the wall is not solely a compositional impact and the solidification conditions must be considered, which will be discussed in Section 4.2. Primary FCC (austenite) solidification is predicted for the multi-track wall fabricated with the torch only set-up (Fig. 11b) which aligns with AF-type solidification observed, indicating the single-axis equilibrium simulations can predict a shift in solidification mode based on as-built composition alone. For the multi-track wall, a considerable amount of nickel was retained compared to the single-track wall at the expense of manganese and iron. The retention of nickel shifts the composition of the wall to a lower Cr_{eq}/Ni_{eq} ratio that favors austenite formation [19]. Note that the nitrogen content among the walls does not vary considerably and is similar to the nitrogen content reported for the feedstock wire, indicating minimal nitrogen pick-up from the atmosphere during fabrication. Although nitrogen is a potent austenite stabilizer, it is not the cause of the solidification mode shift. The deposition of additional beads for the multi-track wall resulted in sufficient elemental vaporization that the final wall composition is drastically different from the initial feedstock composition where the nickel content of the wall is out of the specification limit of 316L (Table 1). This shift in solidification mode would not be realized by using the initial feedstock wire composition for the single-axis equilibrium simulations, indicating the as-built composition is needed to accurately predict solidification mode shifts.

For the single-track and multi-track walls fabricated with the updated shielding gas set-up, the single-axis equilibrium simulations accurately predict primary BCC (δ-ferrite) solidification for both cases (Fig. 11c and Fig. 11d). The addition of three additional shielding gas tubes to the build chamber resulted in different elemental vaporization losses compared to the torch only set-up. An increase in chromium content is observed for both the single-track and multi-track walls along with a large increase in nickel for the single-track wall, similar to the nickel content of the multi-track walls that exhibited AF solidification. Increases in chromium and nickel content in the walls are mostly at the expense of iron. For all the DED-LB walls, iron appears to be preferentially vaporizing out of the melt pool. The predicted temperature difference between BCC and FCC solidification for the single-track wall (Fig. 11c) is small due to the nickel increase, indicating that the δ-ferrite dendrite is just barely chemically stabilized over the austenite dendrite tip. In the etched micrograph in Fig. 5a and Fig. 5d, the underlying austenite dendrite structure is observable. The slight increase in chromium content in the wall was sufficient to stabilize primary δ-ferrite solidification, which the single-axis equilibrium simulation accurately predicted. The relative chemical stability of δ-ferrite compared to austenite would not be distinguishable with just the feedstock composition.

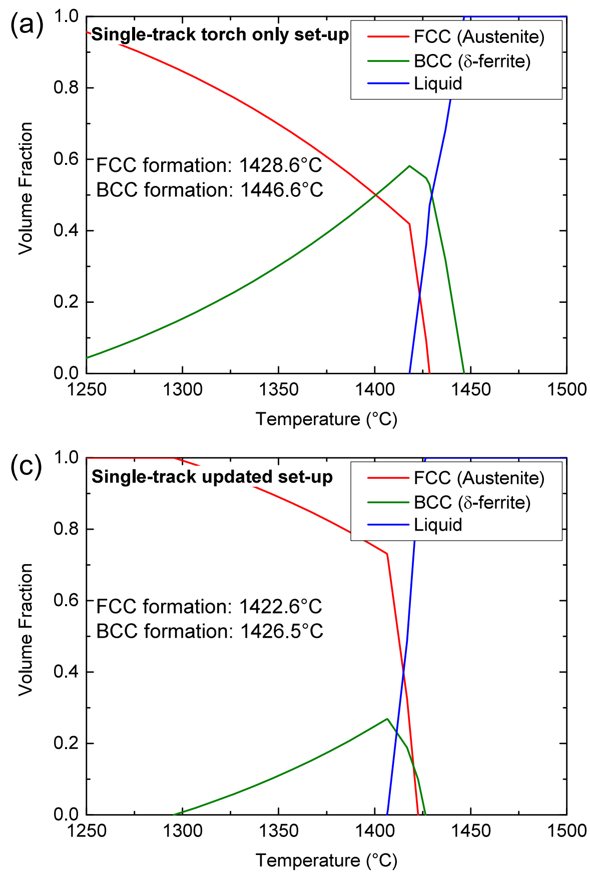

Fig. 11. Single-axis equilibrium simulations of (a) single-track wall fabricated with torch only shielding gas set-up, (b) multi-track wall fabricated with torch only shielding gas set-up, (c) single-track wall fabricated with updated shielding gas set-up, and (d) multi-track wall fabricated with updated shielding gas set-up indicating predicted primary solidification mode.

4.2 Solidification Velocity Impact on Solidification Mode

In addition to composition, solidification conditions such as solidification velocity and cooling rate also impact solidification behavior. For the single-track walls fabricated with torch only shielding gas set-up, the shift in solidification mode within the walls, from FA in the bulk to AF at the top layer, is due to increased solidification velocity at the top of the melt pool. The primary solidification mode is dictated by the phase with the highest dendrite tip temperature and is thus kinetically favored. As solidification velocity increases, the total undercooling (curvature undercooling plus constitutional undercooling) increases, reducing the dendrite tip temperature. High solidification velocities are inherent to most AM processes and for the DED-LB process, the increased solidification velocity at the top of the melt pool provide sufficient dendrite tip undercooling that the temperature of a δ-ferrite dendrite tip can dip below that of an austenite dendrite tip, thus promoting a shift in solidification mode from primary δ-ferrite to primary austenite. This is illustrated in Fig. 12 where austenite and δ-ferrite dendrite tip temperatures are plotted as a function of solidification velocity for different DED-LB wall compositions. The dendrite tip temperature and solidification velocity were calculated using the Ivantsov marginal stability dendrite growth model for rapid columnar growth - KGT model [49,50]. Details of the dendrite tip temperature calculations are provided in Appendix A. As solidification velocity increases, the primary δ-ferrite dendrite tip temperature drops more rapidly, due to larger undercooling, than the primary austenite dendrite tip, and at a critical solidification velocity, the primary δ-ferrite dendrite tip temperature drops more rapidly, due to larger undercooling, than the primary austenite dendrite tip, and at a critical solidification velocity, primary austenite dendrites have the highest dendrite tip temperature. Thus, above a critical solidification velocity, austenite dendrites become more stable over δ-ferrite dendrites, resulting in a shift in solidification mode.

For the single-track wall fabricated with the torch shielding gas set-up, green lines in Fig. 12, the dendrite tip temperature at which the austenite and δ-ferrite intersect is at a high solidification velocity. It is known that thermal gradients and solidification velocities vary within the melt pool of AM builds, where the thermal gradient decreases from the bottom to the top of the melt pool, while solidification velocity increases from the bottom to the top of the melt pool [51]. For single-track walls fabricated with the torch only set-up, the shift in solidification mode from FA to AF-type was only observed at the top layer of the build where the top of the melt pool is preserved, and the fastest solidification conditions exist. Throughout the bulk, where only the bottom of the melt pool is still present, solidification velocities were not fast enough to induce the undercooling needed for AF-type solidification. The stabilization of the austenite dendrite tip at increased solidification velocities is why PBF-LB builds of 316L are typically fully austenitic. Alloys that are expected to solidify as primary δ-ferrite based on composition shift to primary austenite at increased solidification velocities. For the multi-track walls fabricated with the torch shielding gas set-up, blue lines in Fig. 12, the austenite dendrite tip temperature is above the ferrite dendrite tip for all solidification velocities confirming primary austenite solidification is expected for that wall composition. The increase in nickel content chemically stabilized the austenite dendrite tip over the δ-ferrite dendrite tip.

For the single-track wall fabricated with the updated shielding gas, red lines in Fig. 12, the dendrite growth model predicts a shift in solidification mode at a lower velocity than what is predicted for the single-track wall fabricated with the torch set-up. A shift in solidification mode was not observed experimentally indicating improvements to the dendrite growth model are needed for better prediction of solidification mode shifts for a diverse range of build compositions. The dendrite growth model still accurately predicts the overall trend of primary austenite solidification at increased solidification velocities.

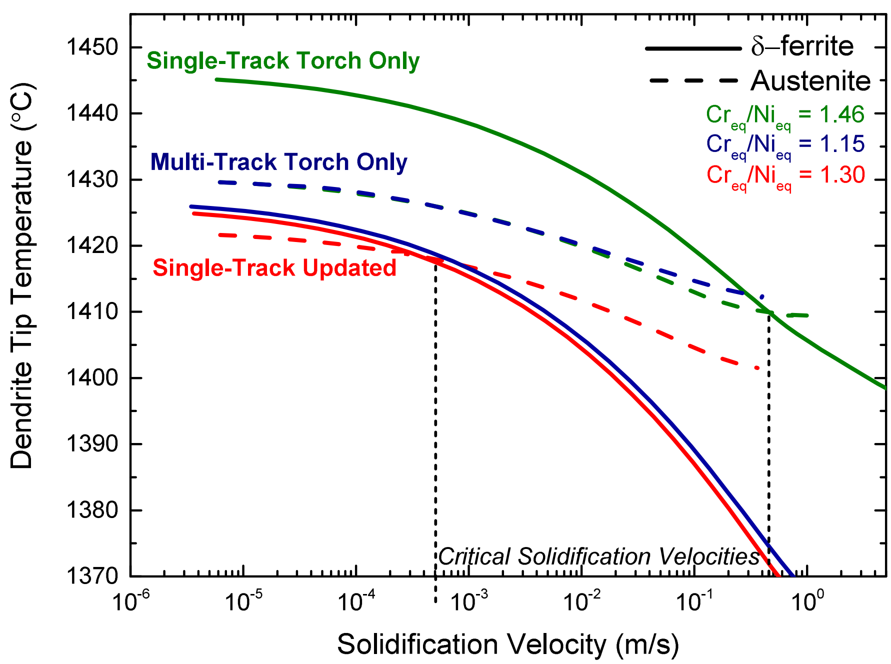

Fig. 12. Dendrite tip temperature as a function of solidification velocity for the DED-LB wall composition calculated using the IMS-KGT model. The solid lines represent the δ-ferrite dendrite tip temperature, and the dashed lines represent the austenite dendrite tip temperature.

While a shift in solidification mode was not observed for the single- and multi-track walls fabricated with the updated shielding gas set-up, a shift in microstructure morphology was, with skeletal δ-ferrite forming in the bulk and lathy δ-ferrite forming at the top layer. Lathy δ-ferrite forms due to fast cooling through the two-phase δ-ferrite plus liquid region to below the δ-ferrite solidus where austenite forms in the solid state [40,41]. Since lathy δ-ferrite is present only in walls fabricated with the updated shielding gas set-up, it can be assumed that the additional shielding gas tubes resulted in an increased cooling rate at the top of the melt pool. Lathy δ-ferrite also appears to alter the solidification texture within the walls (Fig. 8c) due to the K-S OR. The build direction is no longer aligned with {001} solidification texture and there appears to be a breakdown of columnar grains. Lathy δ-ferrite has also been shown to influence the formation of deleterious secondary phases, like sigma, that develop during high temperature applications. The differences in boundary coherency between austenite and lathy or skeletal δ-ferrite impact the precipitation kinetics of sigma phase. The incoherent boundaries between skeletal δ-ferrite and austenite are potent nucleation sites for sigma phase formation compared to the coherent boundaries between lathy δ-ferrite and austenite. It takes longer for sigma phase to form on low-energy, high coherency boundaries when the two phases have an OR. For 304L welds heat treated at 700°C, it was reported that sigma phase nucleation initiated after 32 hours on skeletal δ-ferrite boundaries compared to after 128 hours on lathy δ-ferrite boundaries [33].

5. *Conclusions*

AM 316L material was fabricated via a DED-LB process in which the solidification texture and δ-ferrite morphologies of the walls were used to understand the solidification pathway of the material. The following findings were reported in this work:

- Three solidification morphologies, skeletal δ-ferrite, interdendritic δ-ferrite, and lathy δ-ferrite, and two different solidification modes, FA and AF-type, were observed among the DED-LB walls as a result of variations in wall type and shielding gas set-up that impacted solidification conditions and build composition.
- Skeletal δ-ferrite and interdendritic ferrite exhibited a parallel growth relationship with austenite in which a set of {001} type planes in both phases are parallel. Both the austenite and skeletal δ-ferrite exhibit an {001} solidification texture aligned with the build direction.
- Lathy δ-ferrite is associated with FA-type solidification and forms as a result of plate-like austenite nucleation and growth in the solid state forming Widmanstätten austenite. Lathy δ-ferrite does not have a parallel growth relationship with austenite but rather a K-S OR. The solidification texture of the lathy δ-ferrite and austenite is not well aligned with the build direction.

- Single-axis equilibrium thermodynamic simulations successfully predicted the primary solidification mode of the DED-LB walls based on as-built wall composition. This shift in solidification mode among the walls would not be realized by using the initial feedstock wire composition, indicating the need for as-built composition measurement to predict the solidification mode or final microstructure.
- A shift in solidification mode from the bulk to the top layer was observed for the single-track walls fabricated with the torch only shielding gas set-up. The shift in solidification mode was a result of increased solidification velocity at the top of the melt pool which was preserved only at the top layer of the build. Increased solidification velocity at the top of the melt pool provides sufficient undercooling that the temperature of a δ-ferrite dendrite tip is below the temperature of an austenite dendrite tip thus promoting a shift to primary austenite solidification. This was illustrated by modeling the dendrite tip temperature for each phase for a given wall composition using the IMS-KGT model.

6. Appendix A

6.1 IMS-KGT Solidification Model

The thermal gradient was assumed to be 1.0 x 10^4 k/m for all the calculations based on the fit of the model with experimental data. The objective of this analysis is to calculate dendrite tip temperature as a function of solidification velocity. Ivantsov marginal stability (IMS) for rapid columnar growth (G > 0) of a parabolic needle was solved in the form of a quadratic equation [50]:

$$4\pi^2\Gamma\left(\frac{1}{R^2}\right)+\left(2\sum\left[m_iP_i(1-k_i)C_{l,i}^*\xi_i\right]\right)\left(\frac{1}{R}\right)+G=0 \tag{A.1}$$

where

$$P_i=\frac{RV}{2D_i} \tag{A.2}$$

$$C_{l,i}^*=\frac{C_{o,i}}{1-[(1-k_i)Iv(P_i)]} \tag{A.3}$$

$$\xi_i=1-\frac{k_i}{\sqrt{1+\left(\frac{2\pi}{P_i}\right)^2}-1+2k_i} \tag{A.4}$$

Constants are defined in Table A.1 and values for partitioning coefficient, liquidus slopes, and diffusivity used in the model are included in Tables A.2 – A.4. Single-axis equilibrium Thermo-Calc simulations were used to generate the partitioning coefficients (k_i) and liquidus slopes (m_i) for each solute included in model. The dendrite tip radius (R) was solved for quadratically using equation A.1 for a range of Peclet numbers (P_i). The solidification velocity (V) was then solved for by rearranging equation A.(A.2.

Once the relationship between dendrite tip radius and solidification velocity is understood the total undercooling (ΔT_{total}) can be subtracted from the liquidus temperature to calculate the dendrite tip temperature (T_d):

$$T_d = T_L - \Delta T_{total} \tag{A.5}$$

The total undercooling ahead of a dendrite tip is calculated by summing the undercooling contribution from each solute element (constitutional undercooling, ΔT_c) with the undercooling contribution from a curved interface (curvature undercooling, ΔT_r):

$$\Delta T_{total} = \Delta T_r + \Delta T_c \tag{A.6}$$

where

$$\Delta T_r = \frac{2\Gamma}{R} \tag{A.7}$$

$$\Delta T_{c,i} = m_i(C_{o,i} - C_{l,i}^*) \tag{A.8}$$

For a single build composition, two IMS-KGT modes were generated, one assuming primary δ-ferrite solidification and one assuming primary austenite solidification in order to generate dendrite tip temperature curves for both phases. This was done by removing one of the phases from the Thermo-Calc simulations.

Table A.1
Definition of constants in the IMS-KGT model

Constant	Definition
R (m)	Dendrite tip radius
G (K/m)	Thermal gradient
P_i	Peclet number
Γ (mK)	Gibbs Thomson Coefficient
m_i (K/wt%)	Liquidus slope of solute

k_i	Partitioning coefficient of solute
$C_{o,i}$ (wt%)	Initial composition of solute
D_i (m^2/s)	Solute diffusivity in liquid
T_L (K)	Liquidus temperature
T_d (K)	Dendrite tip temperature
ΔT_{total} (K)	Total undercooling
ΔT_c (K)	Constitutional undercooling
ΔT_r (K)	Curvature undercooling

Table A.2
Partitioning coefficients and liquidus slopes generated from Thermo-Calc assuming primary δ-ferrite solidification and used in IMS-KGT model.

		Cr	Ni	Mo	Mn	Si	N	C
FA	Partitioning Coefficient (k)	1.06	0.72	1.20	0.73	0.69	0.44	0.10
	Liquidus slope (m)	1.66	-7.79	1.4	-5.06	-5.67	-91.75	-137.59
FA/AF	Partitioning Coefficient (k)	1.03	0.75	1.16	0.75	0.73	0.41	0.112
	Liquidus slope (m)	1.34	-7.00	1.40	-5.07	-5.10	-82.95	-126.07
AF	Partitioning Coefficient (k)	1.03	0.74	1.17	0.74	68	0.44	0.10
	Liquidus slope (m)	0.64	-9.11	-1.04	-5.18	-3.41	-82.73	-130.36

Table A.3
Partitioning coefficients and liquidus slopes generated from Thermo-Calc assuming primary austenite solidification and used in IMS-KGT model.

		Cr	Ni	Mo	Mn	Si	N	C
FA	Partitioning Coefficient (k)	0.89	1.00	0.68	0.83	0.93	0.53	0.22
	Liquidus slope (m)	-4.16	-1.35	-5.38	-5.51	-9.90	-19.50	-66.33
FA/AF	Partitioning Coefficient (k)	0.88	1.01	0.69	0.85	0.97	0.55	0.25
	Liquidus slope (m)	-4.43	-1.22	-5.36	-5.01	-3.73	-16.77	-63.25
AF	Partitioning Coefficient (k)	0.89	1.00	0.67	0.83	1.00	0.52	0.23
	Liquidus slope (m)	-4.05	-1.41	-5.38	-5.03	-4.84	-22.00	-65.72

Table A.4
Values use in the IMS-KGT Model [52]

Γ (δ-ferrite)	2.56×10^{-7} mK
Γ (Austenite)	3.22×10^{-7} mK
D (substitutional)	3×10^{-9} m^2/s
D (interstitial)	3×10^{-8} m^2/s

Acknowledgements

This material is based on research sponsored by Army Ground Vehicle Systems Center and Air Force Research Laboratory under agreement number FA8650-20-2-5700. The views and conclusions contained herein are those of the authors and should not be interpreted as necessarily representing the official policies or endorsements, either expressed or implied, of Army Ground Vehicle Services Center, Air Force Research Laboratory or the U.S. Government. Scanning electron microscopy work completed here was supported by National Science Foundation through DMR-1828454. The authors acknowledge OSU (Tate Patterson & Boyd Panton) for insights on DED shielding gas set-up. The authors also acknowledge support from the National Institute of Standards and Technology, USA, US Department of Commerce, USA, for the acquisition of large-scale EBSD during the preparation of this manuscript.

Declaration of Competing Interest

The authors declare that they have no known competing financial interests or personal relationships that could have appeared to influence the work reported in this paper.

CRediT authorship contribution statement

Olivia DeNonno: Conceptualization, Methodology, Software, Validation, Formal Analysis, Investigation, Data Curation, Writing – Original Draft, Writing – Review & Editing, Visualization. **Alec Saville**: Investigation, Validation, Data Curation **Jake Benzing**: Software, Investigation, Resources, Data Curation, Writing – Review & Editing. **Jonah Klemm-Toole**: Conceptualization, Methodology, Formal Analysis, Resources, Writing – Review & Editing, Supervision, Funding acquisition. **Zhenzhen Yu**: Conceptualization, Methodology, Formal Analysis, Resources, Writing – Review & Editing, Supervision, Funding acquisition.

References

[1] W.E. King, A.T. Anderson, R.M. Ferencz, N.E. Hodge, C. Kamath, S.A. Khairallah, A.M. Rubenchik, Laser powder bed fusion additive manufacturing of metals; physics, computational, and materials challenges, Applied Physics Reviews 2 (2015) 041304. https://doi.org/10.1063/1.4937809.

[2] D. Svetlizky, B. Zheng, A. Vyatskikh, M. Das, S. Bose, A. Bandyopadhyay, J.M. Schoenung, E.J. Lavernia, N. Eliaz, Laser-based directed energy deposition (DED-LB) of advanced materials, Materials Science and Engineering: A 840 (2022) 142967. https://doi.org/10.1016/j.msea.2022.142967.

[3] C.R. Cunningham, J.M. Flynn, A. Shokrani, V. Dhokia, S.T. Newman, Invited review article: Strategies and processes for high quality wire arc additive manufacturing, Additive Manufacturing 22 (2018) 672–686. https://doi.org/10.1016/j.addma.2018.06.020.

[4] T. DebRoy, H.L. Wei, J.S. Zuback, T. Mukherjee, J.W. Elmer, J.O. Milewski, A.M. Beese, A. Wilson-Heid, A. De, W. Zhang, Additive manufacturing of metallic components – Process, structure and properties, Progress in Materials Science 92 (2018) 112–224. https://doi.org/10.1016/j.pmatsci.2017.10.001.

[5] M. Ma, Z. Wang, D. Wang, X. Zeng, Control of shape and performance for direct laser fabrication of precision large-scale metal parts with 316L Stainless Steel, Optics & Laser Technology 45 (2013) 209–216. https://doi.org/10.1016/j.optlastec.2012.07.002.

[6] B. Baufeld, E. Brandl, O. van der Biest, Wire based additive layer manufacturing: Comparison of microstructure and mechanical properties of Ti–6Al–4V components fabricated by laser-beam deposition and shaped metal deposition, Journal of Materials Processing Technology 211 (2011) 1146–1158. https://doi.org/10.1016/j.jmatprotec.2011.01.018.

[7] G. George, H. Shaikh, Introduction to Austenitic Stainless Steels, in: Corrosion of Austenitic Stainless Steels, Elsevier, 2002: pp. 1–36. https://doi.org/10.1533/9780857094018.37.
[8] Austenitic Stainless Steels, in: Stainless Steels for Design Engineers, ASM International, 2008: pp. 69–90. https://doi.org/10.31399/asm.tb.ssde.t52310069.
[9] K. Zhang, S. Wang, W. Liu, X. Shang, Characterization of stainless steel parts by Laser Metal Deposition Shaping, Materials & Design 55 (2014) 104–119. https://doi.org/10.1016/j.matdes.2013.09.006.
[10] Z. Wang, T.A. Palmer, A.M. Beese, Effect of processing parameters on microstructure and tensile properties of austenitic stainless steel 304L made by directed energy deposition additive manufacturing, Acta Materialia 110 (2016) 226–235. https://doi.org/10.1016/j.actamat.2016.03.019.
[11] K.A. Sofinowski, S. Raman, X. Wang, B. Gaskey, M. Seita, Layer-wise engineering of grain orientation (LEGO) in laser powder bed fusion of stainless steel 316L, Additive Manufacturing 38 (2021) 101809. https://doi.org/10.1016/j.addma.2020.101809.
[12] A. Röttger, K. Geenen, M. Windmann, F. Binner, W. Theisen, Comparison of microstructure and mechanical properties of 316 L austenitic steel processed by selective laser melting with hot-isostatic pressed and cast material, Materials Science and Engineering: A 678 (2016) 365–376. https://doi.org/10.1016/j.msea.2016.10.012.
[13] J. Yu, M. Rombouts, G. Maes, Cracking behavior and mechanical properties of austenitic stainless steel parts produced by laser metal deposition, Materials & Design 45 (2013) 228–235. https://doi.org/10.1016/j.matdes.2012.08.078.
[14] X. Chen, J. Li, X. Cheng, B. He, H. Wang, Z. Huang, Microstructure and mechanical properties of the austenitic stainless steel 316L fabricated by gas metal arc additive manufacturing, Materials Science and Engineering: A 703 (2017) 567–577. https://doi.org/10.1016/j.msea.2017.05.024.
[15] P. Margerit, D. Weisz-Patrault, K. Ravi-Chandar, A. Constantinescu, Tensile and ductile fracture properties of as-printed 316L stainless steel thin walls obtained by directed energy deposition, Additive Manufacturing 37 (2021) 101664. https://doi.org/10.1016/j.addma.2020.101664.
[16] M. Ziętala, T. Durejko, M. Polański, I. Kunce, T. Płociński, W. Zieliński, M. Łazińska, W. Stępniowski, T. Czujko, K.J. Kurzydłowski, Z. Bojar, The microstructure, mechanical properties and corrosion resistance of 316L stainless steel fabricated using laser engineered net shaping, Materials Science and Engineering: A 677 (2016) 1–10. https://doi.org/10.1016/j.msea.2016.09.028.
[17] P. Ganesh, R. Giri, R. Kaul, P. Ram Sankar, P. Tiwari, A. Atulkar, R.K. Porwal, R.K. Dayal, L.M. Kukreja, Studies on pitting corrosion and sensitization in laser rapid manufactured specimens of type 316L stainless steel, Materials & Design 39 (2012) 509–521. https://doi.org/10.1016/j.matdes.2012.03.011.
[18] X. Chen, J. Li, X. Cheng, H. Wang, Z. Huang, Effect of heat treatment on microstructure, mechanical and corrosion properties of austenitic stainless steel 316L using arc additive manufacturing, Materials Science and Engineering: A 715 (2018) 307–314. https://doi.org/10.1016/j.msea.2017.10.002.
[19] J.C. Lippold, D.J. Kotecki, Welding metallurgy and weldability of stainless steels, John Wiley, Hoboken, NJ, 2005.

[20] M.M. Collur, T. Debroy, Emission spectroscopy of plasma during laser welding of AISI 201 stainless steel, Metall Mater Trans B 20 (1989) 277–286. https://doi.org/10.1007/BF02825608.
[21] A. Block-Bolten, T.W. Eagar, SELECTIVE EVAPORATION OF METALS FROM WELD POOLS, (n.d.) 11.
[22] K. Mundra, T. Debroy, Calculation of weld metal composition change in high-power conduction mode carbon dioxide laser-welded stainless steels, Metall Mater Trans B 24 (1993) 145–155. https://doi.org/10.1007/BF02657881.
[23] C. Hawk, Laser Welding Behavior of Laser Powder Bed Fusion Additive Manufacturing 304L Stainlesss Steel, Colorado School of Mines, 2019. https://www.proquest.com/dissertations-theses/laser-welding-behavior-powder-bed-fusion-additive/docview/2308179156/se-2.
[24] J.W. Elmer, S.M. Allen, T.W. Eagar, Microstructural development during solidification of stainless steel alloys, Metall Mater Trans A 20 (1989) 2117–2131. https://doi.org/10.1007/BF02650298.
[25] S.A. David, J.M. Vitek, R.W. Reed, T.L. Hebble, Effect of rapid solidification on stainless steel weld metal microstructures and its implications on the Schaeffler diagram, 1987. https://doi.org/10.2172/5957599.
[26] J.A. Brooks, A.W. Thompson, Microstructural development and solidification cracking susceptibility of austenitic stainless steel welds, International Materials Reviews 36 (1991) 16–44. https://doi.org/10.1179/imr.1991.36.1.16.
[27] K. Saeidi, X. Gao, Y. Zhong, Z.J. Shen, Hardened austenite steel with columnar sub-grain structure formed by laser melting, Materials Science and Engineering: A 625 (2015) 221–229. https://doi.org/10.1016/j.msea.2014.12.018.
[28] Z. Sun, X. Tan, S.B. Tor, C.K. Chua, Simultaneously enhanced strength and ductility for 3D-printed stainless steel 316L by selective laser melting, NPG Asia Mater 10 (2018) 127–136. https://doi.org/10.1038/s41427-018-0018-5.
[29] J.C. Lippold, Solidification Behavior and Cracking Susceptibility of Pulsed-Laser Welds in Austenitic Stainless Steels, Welding Journal Including Welding Research Supplement 73 (1994) 11.
[30] B. Blinn, P. Lion, O. Jordan, S. Meiniger, S. Mischliwski, C. Tepper, C. Gläßner, J.C. Aurich, M. Weigold, T. Beck, Process-influenced fatigue behavior of AISI 316L manufactured by powder- and wire-based Laser Direct Energy Deposition, Materials Science and Engineering: A 818 (2021) 141383. https://doi.org/10.1016/j.msea.2021.141383.
[31] J.J. Marattukalam, D. Karlsson, V. Pacheco, P. Beran, U. Wiklund, U. Jansson, B. Hjörvarsson, M. Sahlberg, The effect of laser scanning strategies on texture, mechanical properties, and site-specific grain orientation in selective laser melted 316L SS, Materials & Design 193 (2020) 108852. https://doi.org/10.1016/j.matdes.2020.108852.
[32] H. Inoue, T. Koseki, S. Ohkita, M. Fuji, Formation mechanism of vermicular and lacy ferrite in austenitic stainless steel weld metals, Science and Technology of Welding and Joining 5 (2000) 385–396. https://doi.org/10.1179/136217100101538452.
[33] H. Kokawa, T. Kuwana, A. Yamamoto, Crystallographic Characteristics of Delta- Ferrite Transformations in a 304L Weld Metal at Elevated Temperatures, (n.d.) 10.

[34] J. Metelkova, Y. Kinds, K. Kempen, C. de Formanoir, A. Witvrouw, B. Van Hooreweder, On the influence of laser defocusing in Selective Laser Melting of 316L, Additive Manufacturing 23 (2018) 161–169. https://doi.org/10.1016/j.addma.2018.08.006.
[35] E01 Committee, Test Method for Analysis of Austenitic Stainless Steel by Spark Atomic Emission Spectrometry, ASTM International, n.d. https://doi.org/10.1520/E1086-14.
[36] E01 Committee, Test Methods for Determination of Carbon, Sulfur, Nitrogen, and Oxygen in Steel, Iron, Nickel, and Cobalt Alloys by Various Combustion and Fusion Techniques, ASTM International, n.d. https://doi.org/10.1520/E1019-18.
[37] A01 Committee, Specification for Chromium and Chromium-Nickel Stainless Steel Plate, Sheet, and Strip for Pressure Vessels and for General Applications, ASTM International, n.d. https://doi.org/10.1520/A0240_A0240M-22B.
[38] T. Takalo, N. Suutala, T. Moisio, Austenitic solidification mode in austenitic stainless steel welds, MTA 10 (1979) 1173–1181. https://doi.org/10.1007/BF02811663.
[39] H.D. Carlton, A. Haboub, G.F. Gallegos, D.Y. Parkinson, A.A. MacDowell, Damage evolution and failure mechanisms in additively manufactured stainless steel, Materials Science and Engineering: A 651 (2016) 406–414. https://doi.org/10.1016/j.msea.2015.10.073.
[40] J.C. Lippold, W.F. Savage, Solidification of Ausenitic Stainless Steel Weldments: Part 2 - The Effect of Alloy Composition on Ferrite Morphology, Welding Journal 59 (1980) 48s–58s.
[41] N. Suutala, T. Takalo, T. Moisio, Single-phase ferritic solidification mode in austenitic-ferritic stainless steel welds, MTA 10 (1979) 1183–1190. https://doi.org/10.1007/BF02811664.
[42] N. Suutala, T. Takalo, T. Moisio, The relationship between solidification and microstructure in austenitic and austenitic-ferritic stainless steel welds, MTA 10 (1979) 512–514. https://doi.org/10.1007/BF02697081.
[43] S. Kou, Welding Metallurgy, John Wiley & Sons, Inc., Hoboken, NJ, USA, 2002. https://doi.org/10.1002/0471434027.
[44] G.P. Dinda, A.K. Dasgupta, J. Mazumder, Texture control during laser deposition of nickel-based superalloy, Scripta Materialia 67 (2012) 503–506. https://doi.org/10.1016/j.scriptamat.2012.06.014.
[45] D. Ma, A.D. Stoica, Z. Wang, A.M. Beese, Crystallographic texture in an additively manufactured nickel-base superalloy, Materials Science and Engineering: A 684 (2017) 47–53. https://doi.org/10.1016/j.msea.2016.12.028.
[46] M. Gong, Y. Meng, S. Zhang, Y. Zhang, X. Zeng, M. Gao, Laser-arc hybrid additive manufacturing of stainless steel with beam oscillation, Additive Manufacturing 33 (2020) 101180. https://doi.org/10.1016/j.addma.2020.101180.
[47] G. Bouche, J.L. Béchade, M.H. Mathon, L. Allais, A.F. Gourgues, L. Nazé, Texture of welded joints of 316L stainless steel, multi-scale orientation analysis of a weld metal deposit, Journal of Nuclear Materials 277 (2000) 91–98. https://doi.org/10.1016/S0022-3115(99)00134-8.
[48] S. Kang, J.G. Speer, R.W. Regier, H. Nako, S.C. Kennett, K.O. Findley, The analysis of bainitic ferrite microstructure in microalloyed plate steels through quantitative characterization of intervariant boundaries, Materials Science and Engineering: A 669 (2016) 459–468. https://doi.org/10.1016/j.msea.2016.05.111.

[49] R. Trivedi, W. Kurz, Dendritic growth, International Materials Reviews 39 (1994) 49–74. https://doi.org/10.1179/imr.1994.39.2.49.
[50] W. Kurz, D.J. Fisher, R. Trivedi, Progress in modelling solidification microstructures in metals and alloys: dendrites and cells from 1700 to 2000, International Materials Reviews 64 (2019) 311–354. https://doi.org/10.1080/09506608.2018.1537090.
[51] A. Plotkowski, M.M. Kirka, S.S. Babu, Verification and validation of a rapid heat transfer calculation methodology for transient melt pool solidification conditions in powder bed metal additive manufacturing, Additive Manufacturing 18 (2017) 256–268. https://doi.org/10.1016/j.addma.2017.10.017.
[52] T. Umeda, T. Okane, W. Kurz, Phase selection during solidification of peritectic alloys, Acta Materialia 44 (1996) 4209–4216. https://doi.org/10.1016/S1359-6454(96)00038-9.